

WLM-1: A NON-ROTATING, GRAVITATIONALLY UNPERTURBED, HIGHLY ELLIPTICAL EXTRAGALACTIC GLOBULAR CLUSTER

ANDREW W. STEPHENS¹

Gemini Observatory, 670 N. A'ohoku Place, Hilo, HI 96720

MÁRCIO CATELAN

Pontificia Universidad Católica de Chile, Departamento de Astronomía y Astrofísica,
Av. Vicuña Mackenna 4860, 782-0436 Macul, Santiago, Chile

AND

ROXANA P. CONTRERAS

University of Missouri, Department of Physics & Astronomy, 503J Benton Hall, 8001 Natural Bridge Road, St. Louis, MO 63121

Received 2005 Oct 3

ABSTRACT

Globular clusters have long been known for presenting (at times) significant deviations from spherical symmetry. While rotation has been the main proposed explanation, other complicating factors such as their constant interaction with the strong gravitational potential of their host galaxy have made it difficult for a consensus to be reached. To address this question we have obtained high-resolution spectra of WLM-1, the lone globular cluster associated with the isolated, low-mass dwarf irregular galaxy WLM. Using archival HST WFPC2 data, we measure the radial ellipticity profile of WLM-1, finding it to be highly elliptical, with a mean value of 0.17 in the region $0.5 - 5''$ —which is comparable to what is found in our Galaxy for the most elliptical globular clusters. There is no evidence of isophote twisting, except for the innermost regions of the cluster ($r < 0.5''$). To investigate whether the observed flattening can be ascribed to rotation, we have obtained long-slit high-resolution VLT/UVES spectra of this cluster along and perpendicular to the axis of flattening. Using cross-correlation we find that the velocity profile of the cluster is consistent with zero rotation along either axis. Thus neither cluster rotation nor galactic tides can be responsible for the flattened morphology of WLM-1. We argue that the required velocity dispersion anisotropy between the semi-major and semi-minor axes that would be required to account for the observed flattening is relatively small, of order 1 km s^{-1} . Even though our errors preclude us from conclusively establishing that such a difference indeed exists, velocity anisotropy remains at present the most plausible explanation for the shape of this cluster.

Subject headings: galaxies: star clusters — stars: kinematics

1. INTRODUCTION

Globular clusters have long been noted to deviate, sometimes substantially, from perfect spherical symmetry (Shapley 1917; Pease & Shapley 1917). What is the reason why many globular clusters are non-spherical? A conclusive answer to such an important question in the study of globular cluster dynamics, with potentially important ramifications in the study of the evolution of globular cluster stars (Norris 1983, 1987), has so far not been conclusively established (see Meylan & Heggie 1997, for an extensive review and references).

Several possible causes of deviations of globular cluster shapes from sphericity have been suggested, including tidal stresses due to the presence of strong galactic tidal fields (Longaretti & Lagoute 1997; Combes et al. 1999), gravothermal shocks during the passage of a cluster through the disk (Kontizas et al. 1989), velocity anisotropies, and internal rotation (which may also be acquired by interaction with a massive galaxy; Lee et al. 2004 and references therein). In particular, the former two phenomena are now well docu-

mented, with a particularly impressive example being given by Palomar 5 (Odenkirchen et al. 2001). The possibility that rotation may be the main driver of cluster ellipticities (Ryden 1996) is supported by the Meylan & Mayor (1986) and Merritt, Meylan, & Mayor (1997) studies of ω Centauri (NGC 5139), which are based upon a detailed analysis of its structural and dynamical profiles. Yet, it still remains unclear, both from an empirical and from a theoretical perspective, whether rotation can be the main cause of flattening of globular star clusters.

On the observational side, we currently lack detailed velocity profiles for most globular clusters; and even though we do have detailed rotational information for a few clusters, such as 47 Tucanae (NGC 104), ω Cen, M4 (NGC 6121) and M15 (NGC 7078) (Mayor et al. 1984; Gebhardt et al. 1995; Peterson 1995; Gerssen et al. 2002; Zoccali 2004), the lack of a wider sample, as well as of reliable measurements of the variation in flattening as a function of radius for clusters encompassing the full range of observed ellipticities, has hindered further progress in establishing the general correspondence, or lack thereof, between flattening and cluster rotation. Indeed, the latest catalogs of globular cluster ellipticities, published by Frenk & Fall (1982) and by White & Shawl (1987), are entirely based on photographic data, consider exclusively the outermost cluster regions, and, relying on visual data, can be severely affected by differential reddening (van den Bergh

Electronic address: stephens@gemini.edu
Electronic address: mcatelan@astro.puc.cl
Electronic address: rpcontre@astro.puc.cl

¹ Princeton-Católica Fellow at Princeton University Observatory & Pontificia Universidad Católica de Chile during part of this work.

1982). Our group is currently building a new, detailed catalog of globular cluster ellipticities, based on 2MASS (near-infrared) data, which will greatly improve on the current situation (Navarro, Catelan, & Stephens 2006).

Theoretically, too, the case for rotation as one of the main drivers of globular cluster ellipticity is far from being settled. In particular, Meza (2002) has recently argued that globular clusters can rotate to very fast rates without deviating substantially from sphericity. This result is in contrast with those from Alimi & Perez (1999), who instead were unable to produce models of fast-rotating globular cluster-like structures *without* an accompanying deviation from sphericity, in the sense that their modeled structures became lengthened along one or two axes, depending on the initial anisotropy of the velocity distributions.

An ideal test, from an empirical viewpoint, of the impact of rotation on the shapes of globular star clusters, is to measure the rotation velocity of a highly flattened, isolated extragalactic globular cluster, where there is little possibility that tidal effects and/or gravothermal shocks may be responsible for its flattening. The closest possible approximation to such an isolated, flattened system is represented by the single, old globular cluster in the Wolf-Lundmark-Melotte (WLM) dwarf irregular galaxy (DDO 221). While distant (885 kpc; Hodge et al. 1999), the mass of the WLM galaxy is much smaller than even the LMC or SMC, with M_V of -14.4 , -18.5 , and -17.1 , respectively (van den Bergh 2000), thus effectively ruling out the possibility that the non-spherical shape of the WLM cluster (hereafter WLM-1) can be due to tidal effects or gravothermal shocks. Note, in this sense, that this is not necessarily the case even in the Magellanic Clouds (Goodwin 1997), where non-spherical globular clusters of all ages can be found (van den Bergh 1991, and references therein).

In this paper we begin by reanalyzing archival HST WFPC2 data in Section 2, where we measure the ellipticity and surface brightness profiles of WLM-1. We then discuss our new VLT UVES observations and their reduction in Section 3, and attempt to measure the rotation (Section 5) and velocity dispersion (Section 6) of WLM-1. We conclude with a discussion of the possibility of velocity anisotropy in WLM-1 as a possible explanation for its observed morphology, and give some final remarks in Section 9.

2. HST WFPC2 OBSERVATIONS

In order to measure accurate ellipticity and surface brightness profiles of WLM-1, we have downloaded calibrated HST WFPC2 F814W and F555W images from the HST archive (program GO 6813, PI P. W. Hodge). In these images WLM-1 is centered on the PC chip. The only processing required was to combine the two images in each filter to reject cosmic rays. We also combined the images from different filters to reject the remaining few cosmic rays. This final image, rotated to put north at the top, is shown in Figure 1.

2.1. Cluster Ellipticity

The ellipticity and position angle as a function of semi-major axis distance are measured with the Image Reduction and Analysis Facility (IRAF²) routine ELLIPSE, where $\epsilon = 1 - b/a$, and a and b are the semi-major and semi-minor axis lengths respectively. The position angle is the angle

² IRAF is distributed by the National Optical Astronomy Observatories, which are operated by AURA, Inc., under cooperative agreement with the NSF.

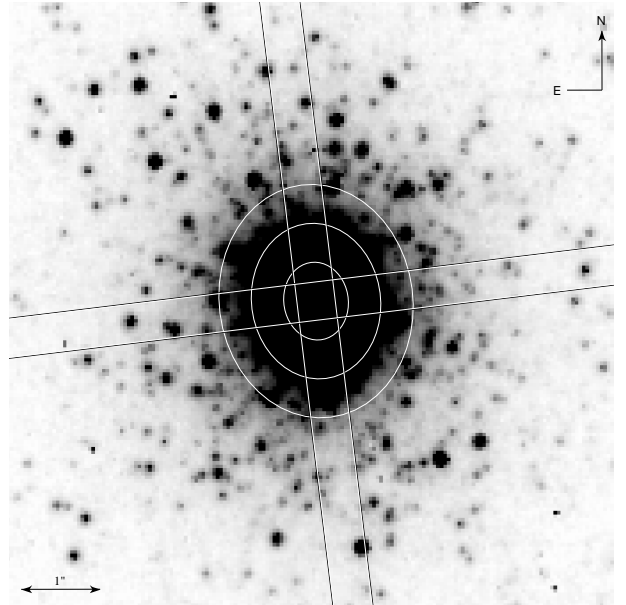


FIG. 1.— A combined F555W/F814W HST image of WLM-1 (Hodge et al. 1999). The approximate size and orientation of the UVES slits are indicated. We have also inscribed ellipses illustrating the mean measured ellipticity (0.17) and position angle (7.1°), and the narrow extraction limits. The size of the image is approximately $7.7''$, north is up and east is left.

($-90^\circ < \alpha < 90^\circ$) made by the major axis measured degrees east of north. The results are illustrated in Figure 2. The mean ellipticities and position angles for our spectral extraction regions are listed in Table 1.

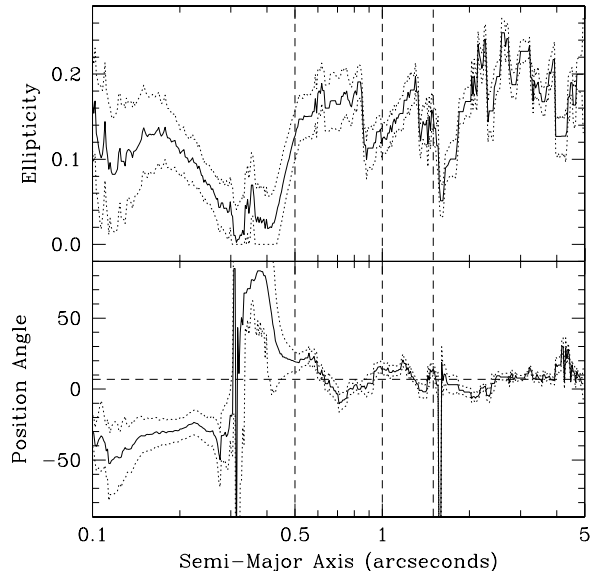


FIG. 2.— Ellipticity and position angle of WLM-1 as a function of semi-major axis distance as measured on the combined F555W and F814W frame. Dotted lines show 1σ measurement errors. Vertical dashed lines at 0.5, 1.0, and $1.5''$ illustrate our spectral extraction limits. The horizontal dashed line indicates the major-axis slit position angle.

Note that since there are many resolved stars in the HST image, there are many irregularities in the measurement of the ellipticity and position angle, especially at larger radii where

TABLE 1
ELLIPTICITY

a''	ϵ	PA($^\circ$)
0.1 – 0.5	0.074 ± 0.042	4.7 ± 44.1
0.5 – 1.0	0.153 ± 0.025	7.0 ± 9.8
1.0 – 1.5	0.150 ± 0.021	9.4 ± 6.5
1.5 – 5.0	0.180 ± 0.038	7.7 ± 6.6

these stars contribute a significant fraction of the total flux (see discussion in Navarro et al. 2005). Also, when the ellipticity gets close to zero (nearly circular), the position angle becomes poorly constrained and shows large fluctuations.

The mean ellipticity of WLM-1 in the region $0.5'' < r < 5''$ is 0.172 ± 0.039 . This ranks among the highest values among Galactic globulars according to the lists tabulated by Frenk & Fall (1982) and White & Shawl (1987), and only ~ 10 Galactic globular clusters have ellipticities greater than this according to the recent analysis of 2MASS data by Navarro et al. (2005). It has previously been noted that LMC and SMC globular clusters of all ages also have significant ellipticities, and in fact tend to be more elliptical than either Galactic or M31 clusters (van den Bergh 1991; Goodwin 1997, and references therein), suggesting an inverse relationship between galaxy mass and globular cluster ellipticity which would appear to be broadly consistent with the case of WLM-1. However, Harris et al. (2002) have recently shown that the giant elliptical galaxy NGC 5128, with $M_V = -20.1$ mag (de Vaucouleurs 1980), also contains a sizable population of flattened clusters.

It is also interesting to note that Han & Ryden (1994) have suggested that, while Galactic and M31 globular clusters shapes are broadly consistent with oblate spheroids, LMC and SMC clusters are instead more consistent with triaxial ellipsoids. As well known, triaxiality is often accompanied by isophote twisting (Williams & Schwarzschild 1979). In the case of WLM-1, we do find some interesting evidence that isophote twisting may indeed be present, but this is clearly restricted to the innermost $0.5''$ of the cluster (Fig. 2).

2.2. Surface Brightness Profile

We have independently measured the surface brightness profile on HST WFPC2 F555W ($\sim V$) and F814W ($\sim I$) images obtained from the HST archive. Using the IRAF ELLIPSE task, with the ellipticity and position angle fixed at the mean values of 0.17 and 7.1° respectively, we measured the average flux in each elliptical annulus, which were then converted to surface brightness using the photometric zero points (ZP) from the HST manual [ZP(555) = 22.545, ZP(814) = 21.639]. The data from the F555W filter are shown as points in Figure 3.

Finally we fit the surface brightness measurements with King (1962) profiles using a chi-squared minimization algorithm and using the RMS scatter in each annulus as an estimate of the measurement errors (although this is actually a measure of the true range of flux values at any particular semi-major axis distance rather than a measure of how accurately one can measure the surface brightness). Pixels within $\sim 0.15''$ of the center of the cluster are saturated, and were therefore excluded from the fit. These excluded points are indicated by open circles in Figure 3. The resulting fits for each

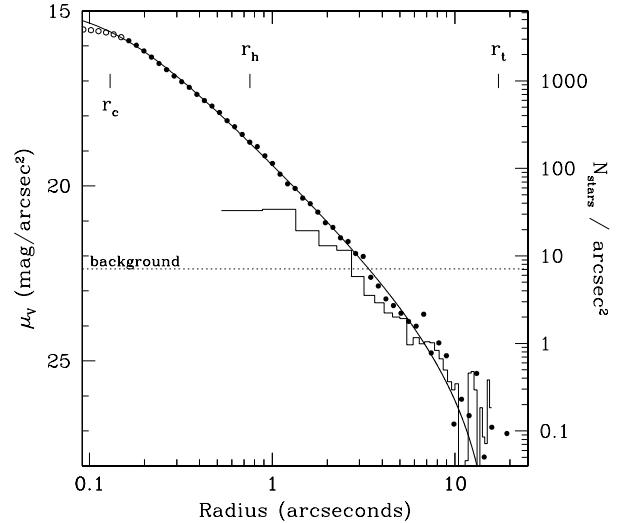


FIG. 3.— The background-subtracted V -band surface brightness profile of WLM-1 (points) and the best-fit King model (line) as determined via chi-squared minimization ignoring the saturated measurements (open points). The fit parameters, core radius (r_c) and tidal radius (r_t), are marked at the top, as well as the background level (dotted line) and the half-light radius (r_h). The background-subtracted star count data from Hodge et al. (1999) have also been overplotted for comparison (histogram), with units shown on the right-hand axis.

filter were then averaged together to give the final values. We find a best-fit core radius of $r_c = 0.126'' \pm 0.021''$, and a tidal radius of $r_t = 16.3'' \pm 10.4''$, where the magnitude of the errors is driven by the large scatter of fluxes in each annulus (due to the resolved nature of the cluster population). The fitting also takes into account the background surface brightness; the best fit values are 22.37 ± 0.13 mag/arcsec 2 in F555W and 21.45 ± 0.13 mag/arcsec 2 in the F814W filter. Note that we have *not* taken into account the finite size of the HST PSF, which has a nominal value of less than $0.1''$ in both filters.

Assuming $(m - M)_0 = 24.73$ (Hodge et al. 1999), one arc-second corresponds to 4.28 parsecs at the distance of WLM-1, and our measurements of the core and tidal radii convert to $r_c = 0.54 \pm 0.09$ pc and $r_t = 70 \pm 44$ pc. Both of these values fall squarely in the range of parameters exhibited by Galactic globulars: $0.03 < r_c(\text{pc}) < 21.9$ and $1.6 < r_t(\text{pc}) < 214$ with median values of $r_c = 1.06$ pc and $r_t = 35.4$ pc (Harris 1996). This implies a very compact globular cluster, with $c \simeq 2.1 \pm 0.3$. We cannot discard the possibility of a collapsed core. Note that our measured half-light radius for the WLM-1 cluster, along with its $M_V = -8.74$ (Sec. 6.1), are not inconsistent with the trend between r_h and M_V for globular clusters in dwarf galaxies and in the outer Galactic halo suggested by van den Bergh & Mackey (2004, their Fig. 7).

The structural parameters of WLM-1 have been previously derived using starcounts by Hodge et al. (1999) who found a core radius of $1.09'' \pm 0.14''$ (4.6 ± 0.6 pc) and a tidal radius of $31'' \pm 15''$ (130 ± 60 pc). A comparison of the background-subtracted star count profile and background-subtracted surface brightness profile (Fig. 3) yields a very good match down to $\sim 2''$, where the star counts start to become incomplete. At $\sim 1''$ the two profiles diverge; the star counts turn over while the surface brightness profile continues to rise down to

TABLE 2
WAVELENGTH COVERAGE

Region	λ_1 (Å)	λ_2 (Å)	Dispersion ^a	Resolution ^b
Blue	3275	4509	0.034	56,700
Red-L	4610	5607	0.038	67,220
Red-U	5682	6650	0.046	66,450

^aÅ/pixel

^b2-pixel resolution

$\sim 0.1''$, at which point the CCD becomes saturated. We speculate that this incompleteness in the star counts is the source of Hodge’s large parameter values.

Other quantities which will be of use later in this paper include the half-light radius r_h , the central V -band surface brightness $\mu_V(0)$, and the mean surface brightness inside the half-light radius $\langle\mu_V\rangle_h$. We estimate these parameters from the best-fit King model to the F555W (V) band HST data. We find: $r_h = 0.75^{+0.27}_{-0.31}$ arcseconds ($3.2^{+1.2}_{-1.3}$ pc), $\mu_V(0) = 14.83^{+0.32}_{-0.46}$ mag/arcsec², and $\langle\mu_V\rangle_h = 17.31^{+0.23}_{-0.50}$ mag/arcsec².

3. VLT UVES OBSERVATIONS

The new data analyzed in this paper were obtained with the UV-Visual Echelle Spectrograph (UVES) on the 8.2 meter VLT UT2 (Kueyen) telescope. UVES is a two-arm cross-dispersed echelle spectrograph with a dichroic splitting the red and blue components of the light. The blue light is recorded on a single $2K \times 4K$ EEV CCD, and the red light on a mosaic of an EEV CCD and an MIT/LL CCD for the reddest orders.

In order to obtain the highest spatial resolution we used a $0.5''$ wide slit, which allows us to obtain velocity information on a similar scale. While slightly undersampling the spectral information, we chose to bin the CCDs 2×2 to improve the signal-to-noise ratio in the faint outer parts of the cluster. This binning yields a plate scale of $0.492''/\text{pixel}$ in the blue and $0.364''/\text{pixel}$ in the red. The blue slit has a length of $8''$ (~ 16 pixels) and the red slit $11''$ (~ 30 pixels). The wavelength coverage and resolution of this configuration is listed in Table 2.

WLM-1 (00:01:49.5, $-15:27:30.7$, J2000) was observed for 3060 seconds in each of two slit positions, one aligned with the major axis (position angle $PA = 6.8^\circ$), and another aligned along the minor axis ($PA = 96.8^\circ$). An HST image of the cluster (Hodge et al. 1999) with the slit orientations indicated is shown in Figure 1.

4. UVES DATA REDUCTION

The data reduction was carried out with IRAF. Each of the three UVES CCDs (Blue, Red-L, Red-U; see Table 2 for wavelength coverages) were reduced independently, beginning with overscan, bias subtraction, and removal of the scattered inter-order light. Before dividing by the flat field, any variations with scales larger than a few pixels were removed from the illuminated regions by fitting and dividing by a high-order spline3 fit using the APFLATTEN task. The resulting “flattened” flat field was then normalized to unity and divided into the science frames. Lastly we located and interpolated over cosmic rays and bad pixels in the science frames using the IRAF median filtering task CRMEDIAN.

The center of the cluster was traced in all orders, and then extracted using the apertures discussed in Section 4.1. The

calibration lamp spectrum and flat field were extracted using identical traces and extraction apertures as the cluster to insure the most accurate wavelength calibration. The extracted science spectra were then divided by the normalized extracted flat field to remove the blaze function and any wiggles due to absorption or emission features in the flat field. Finally we removed any large-scale problems from the extracted spectra, such as bad columns or cosmic ray strikes, using linear interpolation from 100 pixels on either side of the blemish.

The wavelength solution was derived from a Thorium-Argon calibration lamp spectrum. The solutions have an RMS scatter of ~ 0.003 Å, and use ~ 1150 , ~ 750 , and ~ 450 lines in each of the Blue, Red-L, and Red-U wavelength regions respectively. Note that we rederived the wavelength solution for each extraction. We performed one last cleaning of any remaining cosmic rays in the spectra by fitting by a cubic spline of high enough order to fit the absorption features, and iteratively replacing $+4\sigma$ and -6σ outliers with the fit. Finally we trimmed the noise-dominated ends of each order, and combined the orders into a single spectrum

4.1. Extractions

The key to measuring a rotation velocity in data such as these, where a highly concentrated object is barely resolved, is the careful analysis of the light coming from the *edges* of the cluster. While the center of the cluster contains most of the light, and hence has the highest signal-to-noise ratio, the slit of the spectrograph is $0.5''$ wide, thus we can obtain no velocity information in the central $0.5''$. The seeing, which ranged from $0.53''$ to $0.56''$, and the coarseness of our binned pixels ($0.492''/\text{pixel}$ in the blue and $0.364''/\text{pixel}$ in the red) also blur the spatial resolution.

We must therefore concentrate on the outer regions of the cluster. However, the cluster is very compact, with a core radius of $0.126'' \pm 0.021''$ (Sec. 2.2), and the light profile plummets as one moves away from the center; the cluster light fades into the background only $\sim 3''$ from the center.

We have extracted five different regions of various sizes and radii in hopes of obtaining the best measure of the cluster rotation profile. Since the cluster is fairly elliptical ($e \simeq 0.16$ in this region) we scale the minor-axis extraction apertures to insure that we consistently measure the same physical radius of the cluster. The extraction regions are listed in Table 3. The first region includes the entire half of the cluster, and is meant to give a luminosity-weighted rotation estimate. However, as mentioned before, due to the width of the spectrograph slit, the innermost regions will include an equal mix of approaching and receding stars, so the second extraction region excludes the inner $0.5''$. The final three extraction regions are very narrow, and will be used to try to estimate the rotation profile of the cluster.

When possible the extractions use background subtraction, where the background is calculated as the median in two regions on either side of the cluster. These background regions are scaled according to the ellipticity for the minor axes extractions. Note that the slit is too narrow for background subtraction on the blue chip; however, as there are no significant sky lines in the blue, this should not affect the results.

One should note that the WLM-1 cluster is relatively large. The tidal radius is $16'' \pm 10''$ (Sec. 2.2), while the slits used in this paper to obtain the spectra are only $8''$ and $11''$ long. Thus the *entire* slit has contributions from cluster stars, and any attempt at background subtraction will also subtract cluster

TABLE 3
EXTRACTION REGIONS¹

a	Major		Minor	
	Blue	Red	Blue	Red
0.00–1.50''	0.00–3.05	0.00–4.12	0.00–2.56	0.00–3.46
0.50–1.50''	1.02–3.05	1.37–4.12	0.85–2.56	1.15–3.46
0.00–0.50''	0.00–1.02	0.00–1.37	0.00–0.85	0.00–1.15
0.50–1.00''	1.02–2.03	1.37–2.75	0.85–1.71	1.15–2.31
1.00–1.50''	2.03–3.05	2.75–4.12	1.71–2.56	2.31–3.46
background	none	7.20–13.19	none	6.04–11.10

¹Extraction regions in pixels.

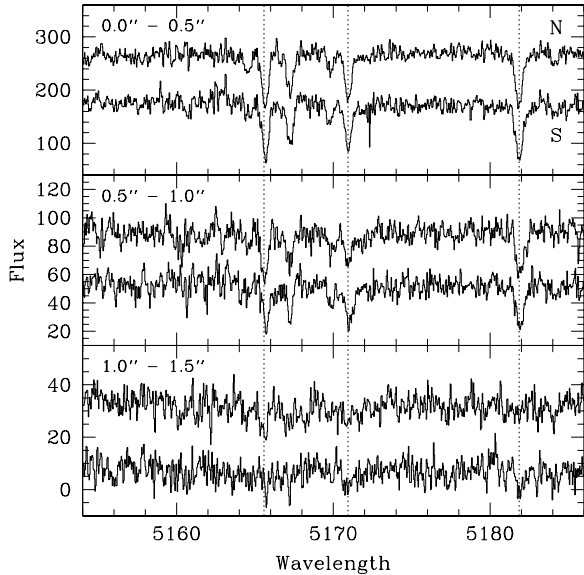


FIG. 4.— Major axis spectra in three different extractions, showing the signal-to-noise level in each. The two spectra in each panel are from the north and south extractions (indicated by “N” and “S”) along the major axis, separated by an equal vertical offset so as not to overlap in this diagram. Any significant rotation would be apparent as a relative shift between these two extractions (a 6.5 km s^{-1} rotation would produce a 13 km s^{-1} shift between the two spectra, corresponding to a 0.22 \AA shift at 5170 \AA). The strong features are Mg I lines (indicated by the vertical dotted lines).

light.

We plot the three narrow spectral extractions along the major axis in Figure 4. This very small piece of the total spectrum illustrates the variation in signal-to-noise ratio with each extraction and the abundance of absorption features available for measuring velocities.

4.2. Atmospheric Absorption

Terrestrial atmospheric absorption lines are noticeable in our Red-U spectra. Two bands are especially strong: H_2O at $5880\text{--}6020 \text{ \AA}$, and O_2 at $6200\text{--}6360 \text{ \AA}$. We did not observe atmospheric standards, and therefore we have no way to accurately correct for this absorption. However, if not removed these absorption lines will bias our Red-U derived rotation velocity toward zero since they are at exactly the same wavelengths on both sides of the cluster.

To remove the telluric absorption lines we simply set any such absorption to the continuum value. We start with a high-

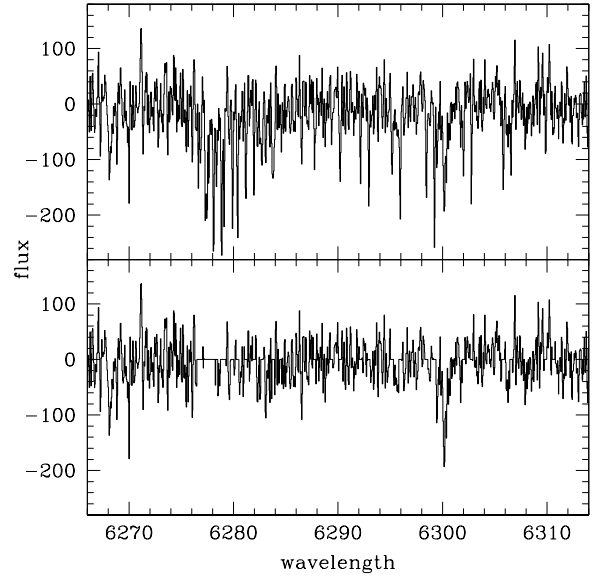


FIG. 5.— Continuum-subtracted WLM-1 major axis spectrum before and after telluric masking in the wavelength region of strong atmospheric O_2 absorption.

resolution atmospheric transmission atlas,³ smooth it to our resolution, and create a “telluric mask” for our spectra. This mask has regions of high transmission set to one, and absorption regions, where the transmission is less than 95%, are set to a very large number. Before cross-correlating the spectra, but after continuum subtraction, we divide by this telluric mask, and effectively set all significant regions of atmospheric absorption to the continuum level. We thus lose any velocity information about WLM-1 which may have been contained in these masked regions, but the cross-correlation will no longer be biased by these strong atmospheric features. A region of telluric absorption is shown in Figure 5 before and after masking.

5. CLUSTER ROTATION

The goal of these observations is to unambiguously measure the rotation velocity of WLM-1. One method of getting an estimate of the magnitude of this rotation would be to follow the original theoretical calculations of King (1961) for the ellipticity of a rotating cluster, which is equivalent to assuming that the cluster is a rotating fluid body. Assuming a distance modulus of $(m-M)_0 = 24.73$ (Hodge et al. 1999), which corresponds to 4.28 pc/arcsec , we find that the rotation velocity of WLM-1 should be of the order

$$v_{\text{rot}} = 6.50 \text{ km s}^{-1} \left(\frac{r}{1''} \right) \left(\frac{\rho'}{10^3 M_{\odot}/\text{pc}^3} \right)^{1/2} \left(\frac{e}{0.16} \right)^{1/2},$$

where ρ' is the effective density calculated for non-homogeneous clusters (van Wijk 1949). Thus if this cluster is indeed elliptical as a result of rotation, we might expect to measure a difference of $\sim 13 \text{ km s}^{-1}$ along the major axis, and zero along the minor axis (see Sec. 6 for a more detailed estimate of the expected rotation).

While our spectra are not of high signal-to-noise ratio, especially in the very narrow extractions, we do have a reasonably

³ ftp.noao.edu/catalogs/atmospheric_transmission

large wavelength coverage. Thus while measuring the position of a single line yields a relatively large error, combining the results for the hundreds of lines present across the spectra increases the precision greatly. One way to simultaneously compare the positions of all features in two spectra is cross-correlation.

We use the Fourier cross-correlation technique of Tonry & Davis (1979), which has been implemented in the IRAF FXCOR task. This routine computes the height, width, and location of the cross-correlation peak of two spectra. For each axis we correlate the north/south (major) and east/west (minor) extractions which lie at equal radii. The results of these correlations for the narrow extractions along both the major and minor axes are shown in Figure 6. The center of the peak is determined by fitting the top 5 points with Gaussian functions. This yields a direct measure of the velocity shift between the two, which is equal to twice the cluster rotation velocity at that distance.

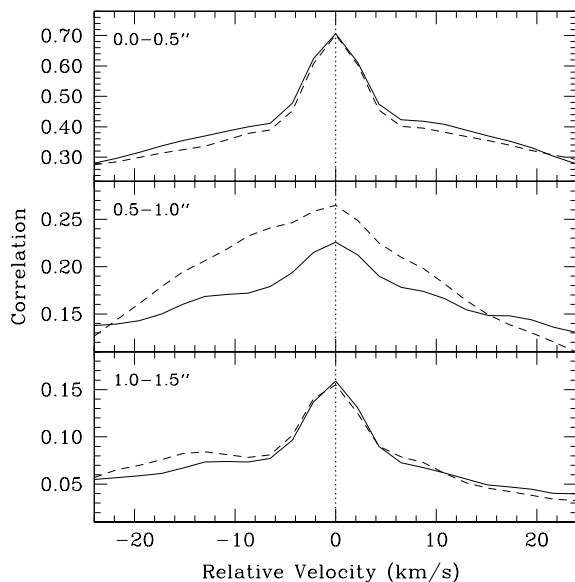


FIG. 6.— Cross-correlation functions measured across the major (solid) and minor (dashed) axes, for each of the three extractions: 0–0.25'' (top), 0.25–0.50'' (middle), and 0.50–1.5'' (bottom).

We start with the reduced, extracted spectra from each chip. In preparation for the cross-correlation we subtract the continuum by fitting with a cubic spline. The telluric absorption is removed from the Red-U spectra following the procedure outlined in Section 4.2. We then cross-correlate the spectra from each (Blue, Red-L, Red-U) chip. Since the reductions, extractions, and wavelength calibrations are completely separate for each chip, this should give three independent, although weaker, measures of the cross-correlation velocity for each extraction. The results of this piecewise cross-correlation are listed in Table 4 for all symmetric extractions, and allow one to compare the quality of the correlation for each chip. We then combine the spectra from all the chips, and cross-correlate the result, excluding the ~ 100 Å gaps between the chips. The results of correlating the combined spectra are listed in Table 5, and shown in Figure 7.

Rather than only make one cross-correlation measurement to obtain the velocity at each radius, we can also cross-correlate all possible permutations, and find the velocities

TABLE 4
PIECEWISE CROSS-CORRELATION VELOCITIES^a

region	0.0–0.5''	0.5–1.0''	1.0–1.5''
MAJOR-AXIS			
Blue	+0.09 ± 0.16	+1.77 ± 0.55	−0.39 ± 1.58
Red-l	−0.20 ± 0.15	−0.28 ± 0.78	+0.38 ± 0.57
Red-u	+0.02 ± 0.11	−0.23 ± 0.73	−0.20 ± 0.40
Combined	−0.09 ± 0.08	−0.17 ± 0.41	−0.17 ± 0.27
MINOR-AXIS			
Blue	−0.02 ± 0.15	−0.38 ± 0.52	−1.48 ± 0.79
Red-L	+0.05 ± 0.16	+0.02 ± 0.65	−0.06 ± 0.54
Red-U	+0.03 ± 0.11	−0.96 ± 0.65	−0.45 ± 0.49
Combined	−0.03 ± 0.08	−0.56 ± 0.32	−0.39 ± 0.31

^aVelocities in km s^{−1}.

TABLE 5
COMBINED-SPECTRUM CROSS-CORRELATION

a	Major		Minor	
	height	velocity ^a	height	velocity
0.00–1.50''	0.68	+0.01 ± 0.08	0.67	−0.01 ± 0.08
0.50–1.50''	0.26	−0.29 ± 0.33	0.28	−0.42 ± 0.28
0.00–0.50''	0.70	−0.09 ± 0.08	0.69	−0.03 ± 0.08
0.50–1.00''	0.23	−0.17 ± 0.41	0.27	−0.56 ± 0.32
1.00–1.50''	0.16	−0.17 ± 0.27	0.16	−0.39 ± 0.31

^aVelocities in km s^{−1}.

TABLE 6
ROTATION VELOCITIES^a

a	Major	Minor
0.00–0.50''	−0.03 ± 0.04	−0.03 ± 0.05
0.50–1.00''	−0.04 ± 0.09	−0.05 ± 0.12
1.00–1.50''	−0.12 ± 0.11	−0.12 ± 0.14

^aVelocities in km s^{−1}.

which are most consistent with all correlations. In other words, cross-correlating the spectrum extracted from r_i and $-r_i$ will give a measure of $2v_i$. However, one can also correlate spectra from different radii, r_i and r_j , to obtain the relative velocity difference Δv_{ij} .

Using all six narrow extractions yields 15 correlation permutations. Thus we have 15 measurements which depend on only three quantities, assuming that we should find equal but opposite velocities at the same radius on either side of the cluster. We solve for the most probable velocities by minimizing the sum of the squares of the deviation of each correlation.

Thus instead of basing a rotation velocity on only one measurement of the cross-correlation of two spectra at equal distances from the cluster center, we measure 15 correlations between all 6 spectral extractions and find the three velocities which are in best agreement with all measurements. These “best fit” rotation velocities are given as a function of semi-major axis distance in Table 6. We find no statistically significant rotation along the line of sight at any distance along either axis of WLM-1.

5.1. Rotation Errors

In order to estimate the robustness of our results we have performed various cross-correlation simulations. All of these

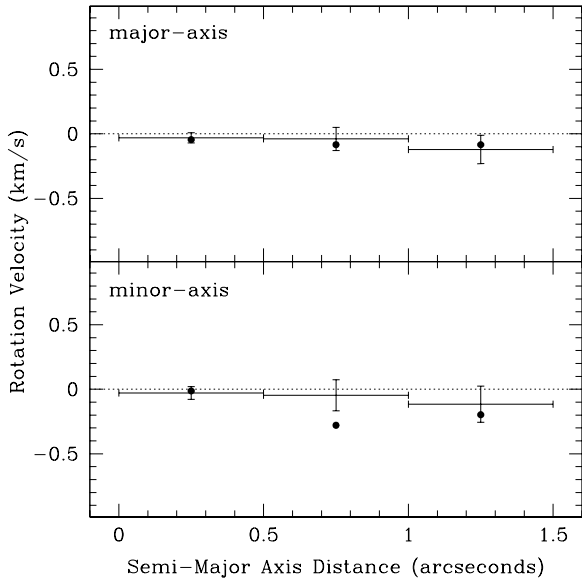


FIG. 7.— Measured cluster rotation along the major (top) and minor (bottom) axes. The points are taken from the last three lines of Table 5 (divided by two to convert to rotation velocity). The data shown by the error bars are the results of simultaneously solving for the best rotation velocities using all 15 narrow extraction cross-correlation permutations (Table 6).

tests start out with a base spectrum which is the average of the major- and minor-axis integrated spectra of WLM-1.

To test the dependence of the cross-correlation velocity on the signal-to-noise ratio of the spectra we create pairs of spectra at various signal levels by adding random noise to two copies of the base spectrum, treating them as opposite sides of the cluster. We then remove the telluric absorption and shift one of the spectra by 5 km s^{-1} . The pair of spectra are then cross-correlated as described in Section 5 to obtain their relative velocity. The results of these tests are illustrated in Figure 8, along with the height and FWHM of the cross-correlation peak. This figure shows no systematic trends with signal-to-noise ratio, and verifies that the velocity errors returned by IRAF are indeed valid. From this analysis we estimate that the errors associated with the measurement of the cross-correlation FWHM are approximately three times the reported velocity errors, and have plotted them as such in Figure 8.

To estimate the errors of the χ^2 -minimization technique used to determine the “best” rotation velocity we ran 50 simulations consisting of six copies of the integrated spectrum of WLM-1 to mimic the six $0.5''$ extractions. Each of the six spectra is shifted such that the simulated cluster has a monotonically increasing rotation velocity with radius, and equal but opposite rotation velocities on opposite sides of the cluster. Specifically, the spectra were shifted by -3 , -2 , -1 , $+1$, $+2$, and $+3 \text{ km s}^{-1}$ each. Noise was added to each spectrum so that the cross-correlation height measured in the simulation (Fig. 8) matched that measured in the real data (columns 2 and 4 in Table 5).

The velocity error distributions (recovered – input) resulting from the 50 simulations have widths of 0.02 , 0.05 , and 0.06 km s^{-1} for the central, middle, and outer velocities respectively. For each simulation we also record the average error of each measurement which results from making all cross-

correlation measurements consistent (the square of this quantity is actually what is minimized when solving for the best set of rotation velocities). The mean of this error over all simulations is 0.031 km s^{-1} . However, in the real data, the error is 0.056 km s^{-1} along the major axis and 0.074 km s^{-1} along the minor axis. This discrepancy indicates that the simulation was too idealistic, and we have therefore scaled the estimated velocity errors by 1.8 for the major axis, and 2.4 for the minor axis, yielding our formal error estimates of 0.04 , 0.09 , and 0.11 km s^{-1} for the central, middle, and outer extractions along the major axis, and 0.05 , 0.12 , and 0.14 km s^{-1} along the minor axis.

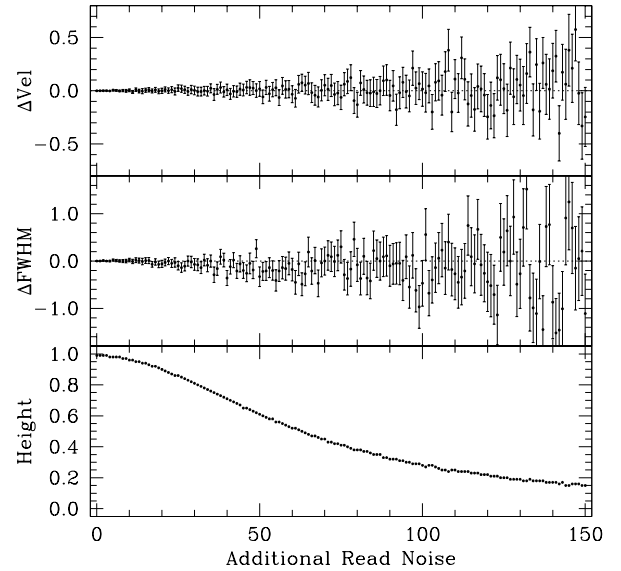


FIG. 8.— Results of cross-correlation simulations using the combined major- and minor- axis integrated spectra with varying amounts of additional random read noise. The spectra were offset by 5 km s^{-1} , and here we illustrate the difference in the cross-correlation velocity (top), and the width (middle) and height (bottom) of the cross-correlation peak. The velocity errors are those returned by FXCOR, and the FWHM errors are three times the velocity error.

6. CLUSTER VELOCITY DISPERSION

The velocity dispersion can be derived from the width of the cross-correlation peak, which is the sum of the line widths of the two spectra being correlated added in quadrature. In the case of the globular cluster WLM-1, the line width is a combination of the intrinsic stellar line width, the instrumental profile, and the velocity dispersion of the cluster. Unfortunately, no template star was measured at the time of our observations.

In order to estimate the velocity dispersion of WLM-1, we used two high-resolution stellar spectra obtained from the UVES Paranal Observatory Project (Bagnulo et al. 2003) as templates. We chose HD 30562 and HD 45067 (both F8V stars) because of their similarities in line strengths to the WLM-1 spectrum. It is important to note that the template spectra were obtained using the $0.5''$ slit and no binning, while the WLM-1 spectra used 2×2 binning. We therefore rebinned the template stars to the same resolution as our observations.

In order to increase the signal-to-noise ratio of the WLM-1 spectra, we averaged together the spectra extracted from opposite sides of the cluster (since we only want to compare the velocity dispersions along the major and minor axes). We

then analyzed the spectra measured on each chip separately to allow optimal Fourier filtering and rejection of undesirable lines. For example, we rejected the blue end of the blue chip which was contaminated by broad hydrogen lines and CaII H&K lines, the region around $H\beta$ on the Red-L chip, and $H\alpha$ on the Red-U chip.

We then cross-correlated each WLM-1 spectrum with each of the two template spectra. This gives a cross-correlation width for each template, which are then averaged. The resulting cross-correlation widths derived for the integrated cluster spectra are 28.7 and 29.0 km s^{-1} for the major and minor axes respectively. This width is the quadratic sum of the WLM-1 and template line widths. In order to estimate the line widths of the templates, we cross-correlate the two templates with one another, and averaging the values from each chip, we find a width of 16.4 km s^{-1} .

If we make the (generous) assumption that the WLM-1 and template spectra have the same instrumental width and intrinsic stellar line widths, it is now possible to subtract these components to find the stellar velocity dispersion. Subtracting in quadrature yields velocity dispersions of 23.5 and 23.9 km s^{-1} along the major and minor axes respectively. Following the same procedure for each of the various spectral extractions of WLM-1 yields the velocity dispersion profile shown in Figure 9, where the errors are three times the velocity errors, as estimated in Section 5.1. Here the extraction semi-major axis distances are shown using flux-weighted centers.

For comparison we have overplotted the velocity dispersion profiles predicted by the isotropic Maxwellian distribution of the King model. These curves show the velocity dispersions computed according to eq. (31) in King (1966) with a concentration $c = 2.00, 2.25,$ and 2.50 , scaled to match the observed central velocity dispersion (but see Sec. 6.1), where the $c = 2.5$ profile is the flattest and, of these three curves, the best fit to the data. The discrepancy between the model and the measured data points (given that the light profile indicates $c = 2.1 \pm 0.3$) suggests that either the mass distribution is more extended than predicted by a King profile or that there is a systematic problem in our measurement of the velocity dispersion.

In order to verify that any observed differences (or lack thereof) in line widths are inherent in the source spectra and not due to changes in the instrumental/atmospheric contribution, we have also compared the widths of unresolved telluric absorption lines in each using the atmospheric transmission spectrum described in Section 4.2 as the template. We first excise a region of each WLM-1 spectrum in the range 6270 – 6320 \AA which is dominated by absorption lines due to atmospheric O_2 . We remove the continuum and broad features by fitting with a high-order cubic spline, and estimate the instrumental width of each via cross-correlation with the atmospheric spectrum. The widths of the telluric lines present in the major- and minor-axis spectra differ by less than 0.05 km s^{-1} , confirming the stability of the conditions during the observations.

Our *absolute* measurement of the velocity dispersion profiles is uncertain due to the low signal-to-noise of our spectra, and the imperfect match with the templates which were obtained at a different time using a different instrument configuration. However, the *relative* velocity dispersion between the major and minor axes should be much more reliable. The bottom of Figure 9 shows the difference between the velocity dispersions measured along the major and minor axes.

All spectral extraction regions are consistent with zero difference, and comparing the integrated cluster spectra measured along the major and minor axes yields a difference of only -0.4 ± 2.6 km s^{-1} (major–minor).

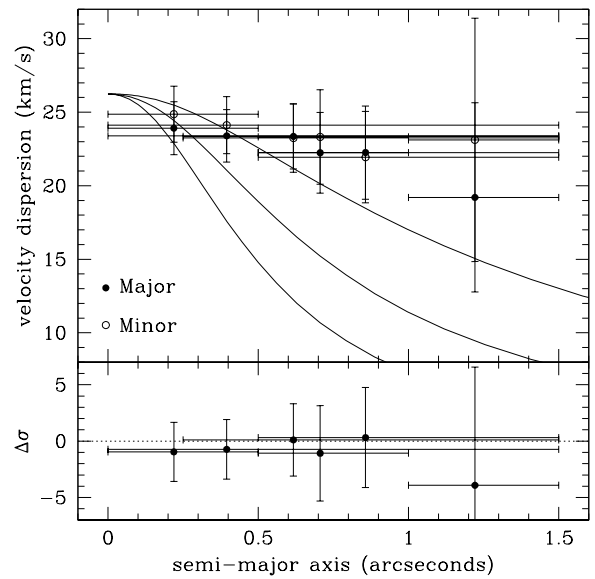


FIG. 9.— The velocity dispersion estimated via cross-correlation along the major-axis (filled circles) and minor-axes (open circles) of WLM-1 (top). The curves show the velocity dispersion profiles predicted by a King model with $c = 2.00, 2.25,$ and 2.50 . The bottom panel shows the difference in velocity dispersion between the major and minor axes.

6.1. Central Velocity Dispersion Estimate

We can obtain an estimate of the central velocity dispersion of WLM-1 as a reality check of our measurement of the velocity dispersion profile. The simplest way to obtain a rough estimate of the velocity dispersion is to utilize the correlation between the central velocity dispersion and the cluster absolute magnitude which was found by Djorgovski et al. (2003) to be followed by globular clusters in several different galaxies. On the basis of Figure 3 (top panel) in Djorgovski et al., we find

$$\log \sigma = -1.01 - 0.229 M_V, \quad (1)$$

where σ is in km s^{-1} . We use the apparent magnitude of the cluster from Table I in Sandage & Carlson (1985), $V = 16.06$ mag, and the extinction and distance moduli estimated by Hodge et al. (1999), $A_V = 0.07$ mag and $(m - M)_0 = 24.73$ mag, respectively, to find $M_V = -8.74$ mag for WLM-1. The above relation then gives a central velocity dispersion $\sigma \simeq 9.8$ km s^{-1} .

A perhaps more accurate estimate for the central velocity dispersion of the cluster can be obtained from the “fundamental plane” correlation for globular clusters, as provided by Djorgovski (1995). In particular, Djorgovski has shown that (Galactic) globulars follow tight relations between the central velocity dispersion σ , the central surface brightness $\mu_V(0)$, and the core radius r_c , on the one hand; and between σ , the half-light radius r_h , and mean surface brightness within r_h , $\langle \mu_V \rangle_h$. Based on his equations (3) and (6), we find:

$$\log \sigma = 4.173(\pm 0.175) + 0.45 \log r_c - 0.204(\pm 0.008) \mu_V(0), \quad (2)$$

and

$$\log \sigma = 4.829(\pm 0.237) + 0.70 \log r_h - 0.244(\pm 0.012) \langle \mu_V \rangle_h, \quad (3)$$

where r_c and r_h are in parsecs, and σ in km s^{-1} .

Using equation (2) with the structural parameters derived in Section 2.2, core radius $r_c = 0.56$ pc and central V -band surface brightness $\mu_V(0) = 14.83$ mag/arcsec², we estimate the velocity dispersion to be $10.8_{-5.3}^{+10.5}$ km s^{-1} . Equation (3) with the half-light radius $r_h = 3.21$ pc and the mean surface brightness inside the half-light radius $\langle \mu_V \rangle_h = 17.31$ mag/arcsec² gives a central velocity dispersion of $9.1_{-5.8}^{+16.3}$ km s^{-1} . These estimates of the central velocity dispersion are lower than our measurements in Figure 9, but the uncertainties do not exclude our value. The larger velocity dispersion implies that the mass of WLM-1 lies on the high side of the relation derived for Galactic clusters.

7. CLUSTER VELOCITY

Extracting an integrated spectrum from the entire cluster using a $3'' (\pm 1.5'')$ aperture yields a relatively high signal-to-noise spectrum relative to the partial extractions used to measure cluster rotation. These integrated spectra have many strong lines from which we can measure the net radial velocity of the cluster. In order to make this measurement, we first calculated and corrected for terrestrial motion, based on the observation times of 2003/10/03 at 3:23 and 4:23 UT for the minor and major-axis respectively. We obtained an atomic line list from Reader & Corliss (1980), and used the IRAF task RVIDLINES to calculate the radial velocity. Centroiding ~ 70 lines in each of the major and minor axis spectra yields heliocentric radial velocities of -105.77 ± 0.50 and -105.84 ± 0.50 km s^{-1} respectively. Averaging the results we estimate that the heliocentric radial velocity of WLM-1 is -105.8 ± 0.4 km s^{-1} . The radial velocity of the WLM galaxy is -116 ± 2 km s^{-1} (Huchra et al. 1993), thus the cluster has a velocity of 10 km s^{-1} with respect to its host.

8. VELOCITY ANISOTROPY

It appears that the ellipticity of WLM-1 cannot be due to rotation, so perhaps WLM-1 is (in a sense) more like elliptical galaxies, where anisotropies in the velocity dispersion play an important role in the observed morphology. To address this hypothesis we employ the tensor virial theorem, as described in Binney & Tremaine (1987), to obtain information about the relation between the ratio of rotation velocity and velocity dispersion v_{rot}/σ , on the one hand, and ellipticity, on the other.

We start by assuming that a globular cluster is an oblate spheroid, rotating around the z axis, and is seen edge-on. We assume, moreover, that the system's isodensity surfaces are concentric ellipsoids. Defining $v_{\text{rot},0}^2$ as the mass-weighted mean-square rotation speed, and σ_0^2 as the mass-weighted mean-square random velocity along the line of sight, we arrive at the following relation:

$$\frac{v_{\text{rot},0}^2}{\sigma_0^2} = \frac{1-\delta}{\sqrt{1-e^2}} \left[\frac{\arcsin(e) - e\sqrt{1-e^2}}{e - \sqrt{1-e^2} \arcsin(e)} \right] - 2, \quad (4)$$

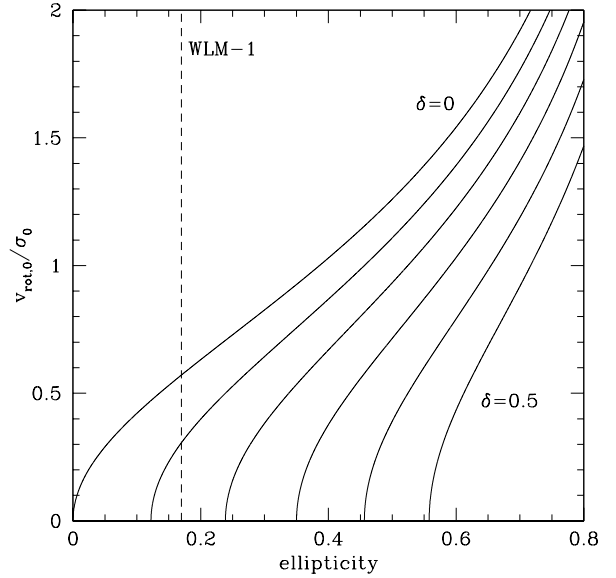


FIG. 10.— The predicted ratio between mass-weighted rotation velocity and mass-weighted velocity dispersion is plotted as a function of the ellipticity for an oblate spheroid. The curves correspond to values of the velocity anisotropy factor δ , with an interval of 0.1 in δ from the upper to the lower curve. The dashed line indicates the measured ellipticity value for WLM-1.

where $\delta < 1$ is a parameter that measures the anisotropy of the velocity dispersion tensor and e is the *eccentricity*, which is related to the ellipticity ϵ as follows:

$$e = \sqrt{1 - (1 - \epsilon)^2}. \quad (5)$$

Using these equations, we can build a family of curves giving $v_{\text{rot},0}/\sigma_0$ as a function of ellipticity for different values of δ . The result is shown in Figure 10. Binney & Tremaine (1987) argue that the representative points in the $(v_{\text{rot}}/\sigma, \epsilon)$ plane of systems that are flattened by rotation lie close to the curve $\delta = 0$, independent of the inclination angle i .

The mean ellipticity of WLM-1, as measured in Section 2.1, is $\epsilon = 0.17$, which is indicated in Figure 10 by the vertical dashed line. As the low mass of the WLM galaxy effectively rules out the possibility that WLM-1 owes its ellipticity to tidal effects or gravothermal shocks, this figure very nicely illustrates the kinematical combinations available to explain the ellipticity of WLM-1.

At one extreme, the ellipticity of WLM-1 could be produced entirely by rotation. In this scenario there is no velocity anisotropy ($\delta = 0$), and reading from the plot, we see that $v_{\text{rot}}/\sigma \approx 0.57$. Taking a conservative estimate of 10 km s^{-1} for the central velocity dispersion of the cluster (Sec. 6), the required rotation would be 5.7 km s^{-1} . However, as we find no measurable rotation ($v_{\text{rot}} \lesssim 0.1$ km s^{-1}), we exclude this possibility.

At the other extreme, the ellipticity of WLM-1 is due entirely to velocity anisotropy. The quantity $(1 - \delta)$, defined as the ratio between the diagonal terms of the velocity dispersion tensor along the rotation (“ z ”) axis and along the elongation (“ x ”) axis, should scale as

$$1 - \delta \approx \sigma_z^2 / \sigma_x^2. \quad (6)$$

From Figure 10, one sees that if there is zero rotation ($v_{\text{rot}}/\sigma =$

0), it is possible to produce the observed ellipticity with a velocity dispersion parameter of $\delta = 0.14$. Therefore, WLM-1's flattening could be accounted for if the velocity dispersion along the rotation axis were smaller than along the elongation axis by

$$\sigma_z \approx 0.93 \sigma_x. \quad (7)$$

Again taking the nominal velocity dispersion to be $\sim 10 \text{ km s}^{-1}$, this velocity anisotropy would only produce a difference of 0.7 km s^{-1} in velocity dispersion between the major and minor axes. Such a difference would be too small to be detected on the basis of our data. Therefore, while we cannot prove that velocity anisotropy is responsible for the observed shape of WLM-1, it certainly appears to be the only option that is consistent with our observations.

9. CONCLUSIONS

We have analyzed VLT UVES long-slit spectra and HST WFPC2 images of the extragalactic globular cluster WLM-1 in an attempt to understand the cause of its elliptical morphology. Unlike the situation for Galactic globular clusters whose detailed shapes may be influenced by their massive host galaxy, WLM is a low-mass dwarf irregular galaxy, eliminating the possibilities that the non-sphericity of WLM-1 could be caused by either tidal stresses or gravothermal shocks. This leaves two explanations for the flattening of this cluster: internal rotation and/or velocity dispersion anisotropy.

Cluster rotation seemed to be a prime candidate for the origin of WLM-1's ellipticity since two-body relaxation, which erases any primordial anisotropy, is relatively efficient in star clusters. In addition, rotation has been measured for several Galactic globular clusters using both proper motion and radial velocity techniques [the review by Meylan & Heggie (1997) lists the rotation velocities of 11 clusters]. The most notable case is that of ω Cen, which exhibits correlated rotation and flattening profiles, strongly suggesting that its ellipticity is due to rotation.

We therefore obtained high-resolution long-slit echelle

spectra along the major and minor axes of the cluster. We used cross-correlation to look for velocity shifts on opposite sides of the cluster, dividing the cluster into annuli in an attempt to obtain a rotation velocity profile. However, we found no evidence for rotation ($v_{\text{rot}} < 0.1 \text{ km s}^{-1}$) along either the major or minor axes of the cluster. As the cluster would require a rotation of $> 6 \text{ km s}^{-1}$ to sustain its shape, we conclude that rotation is definitely not the main driver of WLM-1's ellipticity.

The only remaining plausible source of flattening in the WLM cluster is velocity dispersion anisotropy, the main reason elliptical galaxies are elliptical. We attempted to measure the stellar velocity dispersion in WLM-1 based on the width of the cross-correlation peak; however, due to our large errors, we could see no statistically significant difference between the velocity dispersions measured along the major and minor axes. Calculations reveal that the magnitude of the velocity anisotropy required to produce the observed ellipticity is relatively small: a 7% difference in velocity dispersion, or less than 1 km s^{-1} , which is smaller than our velocity dispersion measurement errors.

In summary, we conclude that the ellipticity of the globular cluster WLM-1 is most likely due to anisotropy in the stellar velocity dispersion.

Support for this work was provided by a Princeton-Católica Prize Fellowship, Proyecto FONDECYT Regular No. 1030976, and a Gemini Science Fellowship (AWS), and by Proyecto FONDECYT Regular No. 1030954 (MC).

Based on observations made with ESO Telescopes at the Paranal Observatories under programme ID 072.D-0355; and with the NASA/ESA *Hubble Space Telescope*, obtained at the Space Science Institute, which is operated by the Association of Universities for Research in Astronomy, Inc., under NASA contract NAS5-26555, retrieved from the ESO ST-ECF Archive.

REFERENCES

- Alimi, J. M., Perez, J., & Serna, A. 1999, *MNRAS*, 305, 859
 Bagnulo, S., Jehin, E., Ledoux, C., Cabanac, R., Melo, C., & Gilmozzi, R. 2003, *Messenger*, 114, 10
 Binney, J., & Tremaine, S. 1987, *Galactic Dynamics* (Princeton University Press, Princeton)
 Combes, F., Leon, S., & Meylan, G. 1999, *A&A*, 352, 149
 de Vaucouleurs, G. 1980, *ApJ*, 240, L93
 Djorgovski, S. 1995, *ApJ*, 438, L29
 Djorgovski, S. G., Côté, P., Meylan, G., et al. 2003, in *New Horizons in Globular Cluster Astronomy*, ASP Conf. Ser., Vol. 296, ed. G. Piotto, G. Meylan, S. G. Djorgovski, & M. Riello (San Francisco: ASP), 479
 Frenk, C. S., & Fall, S. M. 1982, *MNRAS*, 199, 565
 Gebhardt, K., Pryor, C., Williams, T. B., & Hesser, J. E. 1995, *AJ*, 110, 1699
 Gerssen, J., van der Marel, R. P., Gebhardt, K., Guhathakurta, P., Peterson, R. C., & Pryor, C. 2002, *AJ*, 124, 3270
 Goodwin, S. P. 1997, *MNRAS*, 286, 39
 Han, C., & Ryden, B. S. 1994, *ApJ*, 433, 80
 Harris, W. E. 1996 *AJ*, 112, 1487
 Harris, W. E., Harris, G. L. H., Holland, S. T., & McLaughlin, D. E. 2002, *AJ*, 124, 1435
 Hodge, P. W., Dolphin, A. E., Smith, T. R. & Mateo, M. 1999, *ApJ*, 521, 577
 Huchra, J., Latham, D. W., da Costa, L. N., Pellegrini, P. S., & Willmer, C. N. A. 1993, *AJ*, 105, 1637
 King, I. 1961, *AJ*, 66, 68
 King, I. 1962, *AJ*, 67, 471
 King, I. 1966, *AJ*, 71, 64
 Kontizas, E., Kontizas, M., Sedmak, G., & Smareglia, R. 1989, *AJ*, 98, 590
 Lee, K. H., Lee, H. M., Fahlman, G. G., & Sung, H. 2004, *AJ*, 128, 2838
 Longaretti, P.-Y., & Lagoute, C. 1997, *A&A*, 319, 839
 Mayor, M., Benz, W., Imbert, M., et al. 1984, *A&A*, 134, 118
 Meylan, G., & Mayor, M. 1986, *A&A*, 166, 122
 Meylan, G., & Heggie, D. C. 1997, *A&A Rev.*, 8, 1
 Meza, A. 2002, *A&A*, 395, 25
 Merritt, D., Meylan, G., & Mayor, M. 1997, *AJ*, 114, 1074
 Navarro, C., Catelan, M., & Stephens, A. W. 2006, in preparation
 Norris, J. 1983, *ApJ*, 272, 245
 Norris, J. 1987, *ApJ*, 313, 65
 Odenkirchen, M., Grebel, E. K., Rockosi, C. M., et al. 2001, *ApJ*, 548, L165
 Pease, F. G., & Shapley, H. 1917, *Contr. Mt. Wilson Obs.*, 129
 Peterson, R. C., Rees, R. F., & Cudworth, K. M. 1995, *ApJ*, 443, 124
 Reader, J., & Corliss, Ch. H. 1980, *CRC Handbook of Chemistry and Physics*
 Ryden, B. S. 1996, *ApJ*, 461, 146
 Sandage, A., & Carlson, G. 1985, *AJ*, 90, 1464
 Shapley, H. 1917, *Pop. Astronomy*, 25, 374
 Tonry, J., & Davis, M. 1979, *AJ*, 84, 1511
 van den Bergh, S. 1982, *Observatory*, 102, 228
 van den Bergh, S. 1991, *ApJ*, 369, 1
 van den Bergh, S., & Mackey, A. D. 2004, *MNRAS*, 354, 713
 van Wijk, U. 1949, *AnAp*, 12, 81
 White, R. E., & Shawl, S. J. 1987, *ApJ*, 317, 246
 Williams, T. B., & Schwarzschild, M. 1979, *ApJ*, 227, 56
 Zoccali, M. 2004, private communication